Acta Crystallographica Section D
**Biological Crystallography**
ISSN 1399-0047

# Structure of the bifunctional aminoglycoside-resistance enzyme AAC(6′)-Ie-APH(2″)-Ia revealed by crystallographic and small-angle X-ray scattering analysis

**Clyde A. Smith,[a]* Marta Toth,[b] Thomas M. Weiss,[a] Hilary Frase[b] and Sergei B. Vakulenko[b]***

[a]Stanford Synchrotron Radiation Lightsource, Stanford University, Menlo Park, CA 94025, USA, and [b]Department of Chemistry and Biochemistry, University of Notre Dame, Notre Dame, IN 46556, USA

Correspondence e-mail: csmith@slac.stanford.edu, svakulenko@nd.edu

Received 6 June 2014
Accepted 31 July 2014

**PDB reference:** AAC(6′)-Ie, 4qc6

Broad-spectrum resistance to aminoglycoside antibiotics in clinically important Gram-positive staphylococcal and enterococcal pathogens is primarily conferred by the bifunctional enzyme AAC(6′)-Ie-APH(2″)-Ia. This enzyme possesses an N-terminal coenzyme A-dependent acetyltransferase domain [AAC(6′)-Ie] and a C-terminal GTP-dependent phosphotransferase domain [APH(2″)-Ia], and together they produce resistance to almost all known aminoglycosides in clinical use. Despite considerable effort over the last two or more decades, structural details of AAC(6′)-Ie-APH(2″)-Ia have remained elusive. In a recent breakthrough, the structure of the isolated C-terminal APH(2″)-Ia enzyme was determined as the binary $Mg_2GDP$ complex. Here, the high-resolution structure of the N-terminal AAC(6′)-Ie enzyme is reported as a ternary kanamycin/coenzyme A abortive complex. The structure of the full-length bifunctional enzyme has subsequently been elucidated based upon small-angle X-ray scattering data using the two crystallographic models. The AAC(6′)-Ie enzyme is joined to APH(2″)-Ia by a short, predominantly rigid linker at the N-terminal end of a long $\alpha$-helix. This $\alpha$-helix is in turn intrinsically associated with the N-terminus of APH(2″)-Ia. This structural arrangement supports earlier observations that the presence of the intact $\alpha$-helix is essential to the activity of both functionalities of the full-length AAC(6′)-Ie-APH(2″)-Ia enzyme.

## 1. Introduction

The aminoglycoside family of antibiotics have been used for the treatment of serious bacterial infections for more than 70 years (Durante-Mangoni *et al.*, 2009). Streptomycin, originally isolated from the soil bacterium *Streptomyces griseus* in 1943 (Schatz *et al.*, 1944), was the first successful antibiotic effective against tuberculosis. The aminoglycoside family of antibiotics, which includes kanamycin, gentamicin and neomycin, are composed of a central aminocyclitol ring decorated with two or three aminoglycan rings (Supplementary Fig. S1[1]) and are targeted specifically to the 30S ribosome, where drug binding leads to mistranslation of the mRNA (Carter *et al.*, 2000; Karimi & Ehrenberg, 1994). However, as a result of their extensive use, many bacterial isolates have acquired resistance to the aminoglycoside antibiotics, severely compromising their clinical efficacy.

Acquired resistance to the aminoglycosides can occur through mutation of the ribosomal target, increased efflux of the molecules or, more importantly, through enzymatic modification of the drugs. There are now more than 80 bacterial enzymes capable of deactivating the aminoglyco-

---

[1] Supporting information has been deposited in the IUCr electronic archive (Reference: MN5069).

sides, with these enzymes falling into three classes: nucleotidyltransferases (ANTs), phosphotransferases (APHs) and acetyltransferases (AACs) (Davies & Wright, 1997; Smith & Baker, 2002; Vakulenko & Mobashery, 2003; Kim & Mobashery, 2005; Ramirez & Tolmasky, 2010). The APH and ANT enzymes transfer a phosphate and a nucleotidyl group, respectively, derived from ATP or GTP, onto a hydroxyl receptor on the aminoglycoside. The AAC enzymes use acetyl coenzyme A as a co-substrate and catalyze the acetylation of certain amino groups on the drugs. Each class of enzymes can be further divided into subtypes according to the site of modification and the spectrum of aminoglycoside resistance conferred. Broad-spectrum resistance to the aminoglycosides in Gram-positive bacteria is dominated by the bifunctional enzyme AAC(6′)-Ie-APH(2″)-Ia (Ferretti *et al.*, 1986). This enzyme has both acetyltransferase [AAC(6′)-Ie] and phosphotransferase [APH(2″)-Ia] functional domains, being the product of a fusion of two genes into a single open reading frame, and it has been demonstrated that the genes can be separated into the two independent functionalities with little loss of activity (Boehr *et al.*, 2004).

Structural details of a number of monofunctional AAC enzymes have been reported, including AAC(3)-Ia (Wolf *et al.*, 1998), AAC(2′)-Ia (Vetting *et al.*, 2002) and three AAC(6′) enzymes: AAC(6′)-Ib (Maurice *et al.*, 2008; Vetting *et al.*, 2008), AAC(6′)-Ii (Wybenga-Groot *et al.*, 1999) and AAC(6′)-Iy (Vetting *et al.*, 2004). There are three additional unpublished AAC(6′) structures present in the Protein Data Bank (PDB): AAC(6′)-Ig (PDB entry 4f0y; Center for Structural Genomics of Infectious Diseases, unpublished work), AAC(6′)-Ih (PDB entry 4e8o; Center for Structural Genomics of Infectious Diseases, unpublished work) and AAC(6′) from *Legionella pneumophilia* (PDB entry 3f5b; Midwest Center for Structural Genomics, unpublished work). The AAC(6′) enzymes are members of the large GCN5-related *N*-acetyltransferase (GNAT) family (Dyda *et al.*, 2000; Vetting *et al.*, 2005), which also includes histone acetyltransferase (Hat1; Dutnall *et al.*, 1998), serotonin *N*-acetyltransferase (Hickman *et al.*, 1999) and glyphosate *N*-acetyltransferase (GAT; Siehl *et al.*, 2007), along with the other aminoglycoside acetyltransferase variants AAC(1), AAC(3) and AAC(2′) (Smith & Baker, 2002). The GNAT enzymes can be identified by the presence of a number of conserved sequence motifs, one of which is a glycine-rich loop connecting a $\beta$-strand and an $\alpha$-helix which forms specific hydrogen-bonding interactions with the diphosphate moiety of the acetyl-CoA cofactor reminiscent of the Rossmann dinucleotide-binding motif.

Despite it being the most important enzyme with respect to acquired resistance to aminoglycosides, the three-dimensional structure of AAC(6′)-Ie-APH(2″)-Ia remains elusive. A recent small-angle X-ray scattering (SAXS) study of the full-length homology model of the enzyme has been reported (Caldwell & Berghuis, 2012), suggesting that the bifunctional enzyme may adopt a rigid conformation in solution. In the absence of structural information on the two functional domains of AAC(6′)-Ie-APH(2″)-Ia, the available structures of AAC(6′)-Ib and APH(2″)-IIa were used to construct homology models of the bifunctional enzyme. Rigid-body modeling suggested that the AAC and APH domains were oriented such that the substrate-binding sites were adjacent to one another. More recently, the structure of the APH(2″)-Ia domain of the bifunctional enzyme was reported as the $Mg_2GDP$ complex (Smith *et al.*, 2014). Here, we report the structure of the ternary kanamycin/coenzyme A complex of the AAC(6′)-Ie domain of this enzyme refined at 1.3 Å resolution. This structure, together with the structure of APH(2″)-Ia, is used in conjunction with SAXS data to revisit the modeling of the full-length bifunctional enzyme.

## 2. Materials and methods

### 2.1. Cloning of the *aac(6′)-Ie* gene for protein expression

The gene for the AAC(6′)-Ie domain (amino-acid residues Met1–Tyr179) of the bifunctional AAC(6′)-Ie/APH(2″)-Ia enzyme was PCR-amplified using the sequence of the bifunctional enzyme as a template. During amplification, *Nde*I and *Hin*dIII sites were introduced at the 5′ and 3′ ends of the gene, respectively. The amplified DNA was cleaned on preparative agarose gel, digested with *Nde*I and *Hin*dIII and ligated between the *Nde*I and *Hin*dIII sites in the polylinker of the pET-22b(+) expression vector to generate the pET22::*aac(6′)-Ie* plasmid. The DNA sequence was subsequently verified. After transformation of plasmid DNA into *Escherichia coli* BL21 (DE3) cells, clones were selected on LB agar plates supplemented with 100 µg $ml^{-1}$ ampicillin.

### 2.2. Purification of AAC(6′)-Ie

*E. coli* BL21 (DE3) cells harboring the pET22::*aac(6′)-Ie* plasmid were cultured at 37°C in 200 ml LB medium with 100 µg $ml^{-1}$ ampicillin until an optical density of 0.6 at 600 nm was reached. Protein expression was induced with 0.6 m*M* IPTG and the bacteria were grown overnight at 22°C. Soluble proteins were extracted from the cells as reported previously (Toth *et al.*, 2009). The AAC(6′)-Ie enzyme was first purified by DEAE anion-exchange chromatography and eluted with an NaCl gradient. Fractions were analyzed by 12% SDS–PAGE and protein-containing fractions were dialyzed against 25 m*M* HEPES buffer pH 7.5 and further purified on an Affi-Gel 15/kanamycin affinity column. Bound proteins were eluted with a 0–5 m*M* kanamycin gradient. Fractions containing homogeneously pure AAC(6′)-Ie enzyme were collected, dialyzed, concentrated and stored in liquid nitrogen. Protein concentration was determined according to the optical density at 280 nm using the molecular mass (21 705 Da) and theoretical extinction coefficient (41 892 $M^{-1}$ $cm^{-1}$). Protein solutions destined for SAXS analysis were dialyzed exhaustively against 25 m*M* HEPES pH 7.5 and then centrifuged at 14 000*g* for 10 min just prior to measurement to minimize aggregation.

### 2.3. Small-angle X-ray scattering

SAXS experiments were performed on the Bio-SAXS beamline BL4-2 at Stanford Synchrotron Radiation Lightsource (SSRL; Smolsky *et al.*, 2007). Data were collected using a Rayonix MX225-HE CCD detector (Rayonix, Evanston, Illinois, USA) with a 1.7 m sample-to-detector distance and a beam energy of 11 keV (wavelength $\lambda$ = 1.127 Å). SAXS data were measured in the range $0.0059 \leq q \leq 0.53$ Å$^{-1}$ [$q = 4\pi\sin(\theta)/\lambda$, where $\theta$ is the scattering angle]. The $q$ scale was calibrated with silver behenate powder and the water scattering intensity was used for absolute intensity scaling. Solution SAXS data were collected separately for AAC(6′)-Ie and APH(2″)-Ia as well as for the full-length bifunctional enzyme AAC(6′)-Ie-APH(2″)-Ia in 25 m*M* HEPES pH 7.5. For each of the proteins, a series of five different concentrations was measured ranging from 0.5 to 5 mg ml$^{-1}$ (0.5, 0.75, 1.0, 2.0 and 5.0 mg ml$^{-1}$) in order to detect (and eliminate) concentration-dependent intermolecular interactions. In the case of the AAC(6′)-Ie and the bifunctional enzyme an additional high concentration was measured at 10 and 8 mg ml$^{-1}$, respectively. A series of 15 1 s exposures was taken, analyzed for effects of radiation damage, scaled according to the transmitted intensity and averaged using *SasTool* (Liu, 2009). The scaled and averaged buffer curve was then subtracted from the averaged protein curves. Low- and high-concentration data were then merged to give a single SAXS profile for each of the three proteins. A summary of the SAXS parameters is given in Table 1.

**Table 1**
Small-angle X-ray scattering parameters.

| | AAC(6′)-Ie | APH(2″)-Ia | Bifunctional |
|---|---|---|---|
| Data-collection parameters | | | |
| Instrument | SSRL BL4-2 | SSRL BL4-2 | SSRL BL4-2 |
| Defining slits size, H (mm) × V (mm) | 0.3 × 0.3 | 0.3 × 0.3 | 0.3 × 0.3 |
| Detector distance (m) | 1.7 | 1.7 | 1.7 |
| Wavelength (Å) | 1.127 | 1.127 | 1.127 |
| Energy (keV) | 11 | 11 | 11 |
| $q$ range (Å$^{-1}$) | 0.0059–**0.53** | 0.0059–**0.53** | 0.0059–**0.53** |
| Exposure time per frame (s) | 1 | 1 | 1 |
| Frames per concentration | 15 | 15 | 15 |
| Measured concentrations (g l$^{-1}$) | 0.5, 0.75, 1.0, 2.0, 5.0, 10.0 | 0.5, 0.75, 1.0, 2.0, 5.0 | 0.5, 0.75, 1.0, 2.0, 5.0, 8.0 |
| Temperature (K) | 293 | 293 | 293 |
| Structural parameters | | | |
| $I(0)$ from Guinier at 0.5 g l$^{-1}$ (cm$^{-1}$) | $7.22 \times 10^{-3}$ | $14.9 \times 10^{-3}$ | $19.4 \times 10^{-3}$ |
| $R_g$ from Guinier (Å) | 16.7 | 21.7 | 29.9 |
| Molecular weight from Guinier $I(0)$ (kDa) | 21.4 | 44.2 | 57.3 |
| $q_{\min}R_g$–$q_{\max}R_g$ for Guinier | 0.17–1.29 | 0.13–1.28 | 0.26–1.29 |
| No. of points for Guinier | 73 | 59 | 38 |
| $R_g$ from $P(r)$ (Å) | 16.8 | 22.0 | 30.1 |
| $D_{\max}$ from $P(r)$ (Å) | 48.1 | 65.5 | 94.7 |
| $\chi$ from *CRYSOL* fit | 2.37 | 3.67 | 2.40† |
| Software | | | |
| Primary data reduction | *SasTool* | *SasTool* | *SasTool* |
| *Ab initio* analysis | — | — | *GASBOR* |
| Validation and averaging | — | — | *DAMAVER* |
| Rigid-body modeling | — | — | *CORAL* |
| Computation of model intensities | *CRYSOL* | *CRYSOL* | *CRYSOL* |

† Using the output of the *CORAL* calculation with a flexible linker of six residues.

**Table 2**
Crystallographic data-collection and refinement statistics.

Values in parentheses are for the highest resolution shell.

| | |
|---|---|
| Data collection | |
| Space group | $P2_12_12_1$ |
| Unit-cell parameters (Å) | $a$ = 52.83, $b$ = 89.72, $c$ = 96.96 |
| Resolution (Å) | 19.9–1.30 (1.35–1.30) |
| Reflections (observed/unique) | 561207/112448 |
| $R_{\rm merge}$ (%) | 6.4 (37.1) |
| $\langle I/\sigma(I)\rangle$ | 13.1 (2.4) |
| Completeness (%) | 98.7 (87.2) |
| CC$_{1/2}$† | 99.8 (87.7) |
| Multiplicity | 5.3 |
| Wilson $B$ value (Å$^2$) | 14.6 |
| Refinement | |
| $R_{\rm work}/R_{\rm free}$ (%) | 14.66/16.61 |
| $R_{\rm all}$‡ (%) | 14.76 |
| Reflections used ($R_{\rm all}/R_{\rm free}$) | 112422/5671 |
| Protein/solvent atoms | 3212/725 |
| Average $B$ (Å$^2$) | |
| Protein | 15.8/17.4 |
| Solvent | 29.7 |
| R.m.s.d., bonds (Å) | 0.006 |
| R.m.s.d., angles (°) | 1.29 |
| Ramachandran plot (%) | |
| Most favoured regions | 88.7 |
| Additionally allowed regions | 10.7 |

† CC$_{1/2}$ is the correlation between random half-sets of data (Karplus & Diederichs, 2012). ‡ Calculated using all reflections at the completion of refinement.

### 2.4. Crystallization, diffraction data collection and processing

Initial coarse screens for apo and kanamycin-complexed AAC(6′)-Ie were performed with commercially available sparse-matrix screens (Crystal Screen, Crystal Screen 2, PEG/Ion and PEG/Ion 2, Hampton Research) using the sitting-drop method. Crystals were grown at 4°C in Intelli-Plates (Art Robbins Instruments) using a reservoir volume of 80 µl and drops comprising 1 µl protein-complex solution and 1 µl reservoir solution. Crystals of apo-AAC(6′)-Ie grew from one condition (0.2 *M* ammonium sulfate, 0.1 *M* MES pH 6.5, 30% PEG monomethyl ether 5000), while two conditions gave rise to crystals of the enzyme–kanamycin–coenzyme A ternary complex (0.2 *M* ammonium sulfate, 0.1 *M* MES pH 6.5, 30% PEG monomethyl ether 5000 and unbuffered 0.2 *M* ammonium formate, 20% PEG 3350). Crystals were passed through a cryoprotectant solution containing crystallization buffer supplemented with 20% glycerol, flash-cooled in liquid nitrogen and stored in a sample cassette designed for use with the Stanford Automated Mounting (SAM) system (Cohen *et al.*, 2002) for subsequent diffraction-screening experiments.

Initial screening of the crystals for diffraction quality was carried out on SSRL beamline BL9-2 using the Stanford Auto Mounter (SAM) robotic system (Cohen *et al.*, 2002). The best diffraction quality was obtained from crystals of the AAC(6′)-Ie complex grown in unbuffered 0.2 *M* ammonium formate, 20% PEG 3350. A complete data set was collected from a single crystal on SSRL beamline BL12-2 using a Pilatus 6M pixel-array detector. A total of 750 images were collected with an oscillation angle of 0.2° and an exposure time of 0.2 s per image. The crystal belonged to space group $P2_12_12_1$, with unit-cell parameters $a = 52.83$, $b = 89.72$, $c = 96.96$ Å, and diffracted to approximately 1.3 Å resolution. The data were processed with *XDS* (Kabsch, 1993) and scaled using *SCALA* (Evans, 2006) from the *CCP*4 package (Winn *et al.*, 2011). Table 2 gives a summary of the data-collection statistics.

### 2.5. Structure solution and refinement

The AAC(6′)-Ie structure was solved by molecular-replacement calculations with *MOLREP* (Vagin & Teplyakov, 2010) using the structure of AAC(6′)-Ib (Vetting *et al.*, 2008) as a search model. Calculation of the Matthews coefficient ($V_{\rm M}$), assuming the presence of two molecules in the asymmetric unit, gave a value of 2.65 $Å^3$ $Da^{-1}$, which corresponds to 54% solvent content. All solvent molecules and ligands were removed from the search model and it was converted to a pseudo-AAC(6′)-Ie model using *CHAINSAW* (Stein, 2008), in which identical residues in the two sequences were retained and those which differed were truncated at the $C^{\beta}$ atom. A strong MR solution gave the position of the two AAC(6′)-Ie molecules in the asymmetric unit. The molecular-replacement solution was initially refined using *REFMAC* (Murshudov *et al.*, 2011), and $2F_{\rm o} - F_{\rm c}$ and $F_o - F_c$ electron-density maps were calculated and inspected. Refinement of the structure was completed with the *PHENIX* suite of programs (Adams *et al.*, 2010), and manual building of the model was performed using the molecular-graphics program *Coot* (Emsley & Cowtan, 2004). Water molecules were added at structurally and chemically relevant positions, and the atomic displacement parameters (ADPs) for all nonsolvent atoms in the structure were refined anisotropically. Final refinement statistics are given in Table 2.

The atomic coordinates and the structure factors for kanamycin–coenzyme A–AAC(6′)-Ie were deposited in the Protein Data Bank (Berman *et al.*, 2000) with PDB code 4qc6. Superpositions were performed using the *SSM* procedure (Krissinel & Henrick, 2004) as implemented in *Coot* (Emsley & Cowtan, 2004) and using *LSQKAB* from the *CCP*4 suite (Winn *et al.*, 2011). Figures were generated using *PyMOL* (DeLano, 2002). Electrostatic calculations were carried out with *APBS* (Baker *et al.*, 2001) *via* the *PDB2PQR* server (Dolinsky *et al.*, 2004).

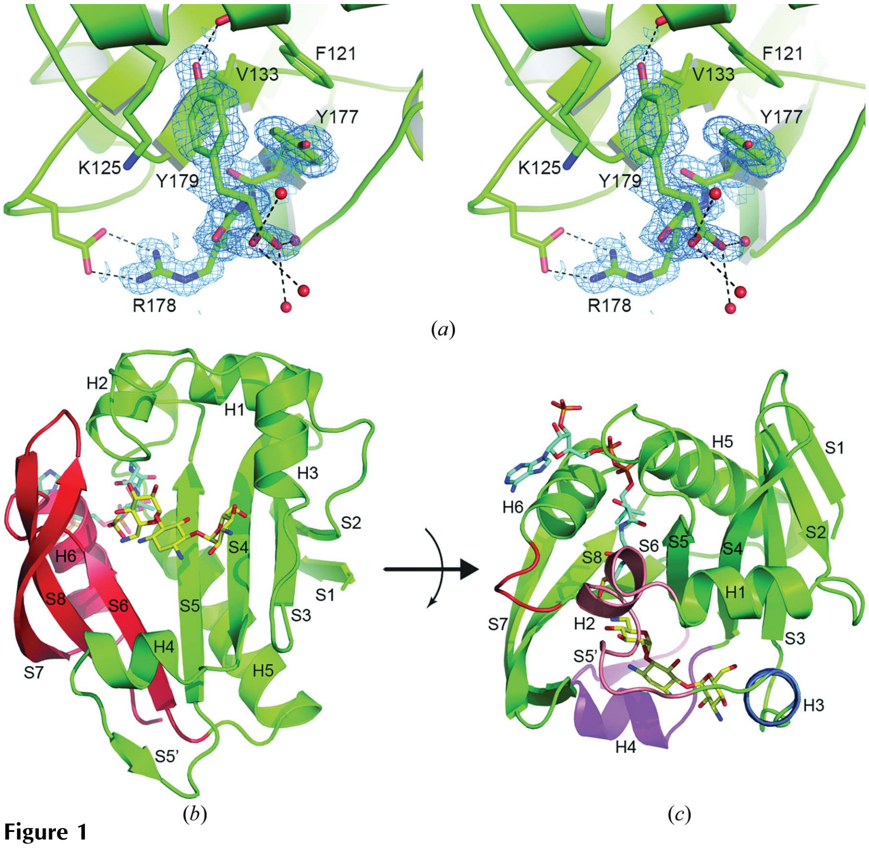

**Figure 1**
(*a*) Stereoview of representative final $2F_{\rm o} - F_{\rm c}$ electron density near the C-terminus of AAC(6′)-Ie contoured at 1.0σ. (*b*) Ribbon representation of the isolated AAC(6′)-Ie showing the secondary-structure numbering. The N-terminal region is colored green and the C-terminal region is colored red. The oxidized coenzyme A is shown as cyan sticks and the kanamycin substrate is shown as yellow sticks. (*c*) View of the AAC(6′)-Ie monomer rotated 90° about a horizontal axis as indicated. The differences in coloring indicate regions of the structure where there are major conformational differences when compared with the structures of other AAC(6′) enzymes: helix H2 (dark pink), helix H3 (blue), helix H4 and strand S5′ (magenta) and the S6–H6 loop (red).

## 3. Results and discussion

### 3.1. Crystal structure of AAC(6′)-Ie

The structure of AAC(6′)-Ie was solved by molecular-replacement (MR) methods using the structure of AAC(6′)-Ib (Vetting *et al.*, 2008) as the starting model and was refined at 1.3 Å resolution (Table 2). The final $2F_{\rm o} - F_{\rm c}$ electron density in the vicinity of the C-terminus and the central hydrophobic core of the molecule is shown in Fig. 1(*a*). The final model comprises residues 1–179 in both molecules in the asymmetric unit. Analysis of the asymmetric unit and the contents of the unit cell indicate that the two independent molecules do not form a noncrystallographic dimer, and the calculation of a self-rotation function also shows no evidence for the presence of a noncrystallographic dyad. It has been reported that other aminoglycoside acetyltransferases and GNAT enzymes have the potential to form physiological dimers, and these have been observed crystallographically (Burk *et al.*, 2003), although it appears that AAC(6′)-Ie is a member of the subset of GNAT enzymes which exist as monomers. Superposition of the two molecules in the asymmetric unit gives a root-mean-square deviation (r.m.s..d) of 0.3 Å for all 179 residues, and inspection of the resulting structural overlap indicates that the backbone conformation of the two AAC(6′)-Ie monomers is essentially identical.

The AAC(6′)-Ie monomer is shown in Figs. 1(*b*) and 1(*c*) in two orientations. For simplicity, the molecule can be viewed as two structural domains: an N-terminal domain comprising strands S1–S5 and helices H1–H5, and a C-terminal domain consisting of strands S6–S8 and helix H6 (Fig. 1*b*). Although the N-domain and C-domain *β*-strands are almost aligned to form a contiguous eight-stranded central *β*-sheet, a divergence of the S5 and S6 strands causes the sheet to adopt a distinct V-shape (Fig. 1*b*). Superposition of AAC(6′)-Ie onto the three other AAC(6′) enzymes for which structures have been reported gives r.m.s.d.s of 1.9, 2.3 and 2.8 Å for AAC(6′)-Ib, AAC(6′)-Ii and AAC(6′)-Iy, respectively. Seven of the eight *β*-strands and five of the six *α*-helices are conserved in all four molecules (Fig. 2). AAC(6′)-Ie has two short strands at the N-terminus whereas the other three enzymes have a single strand, and all four molecules differ to varying degrees at their C-termini: AAC(6′)-Ie and AAC(6′)-Ii have a short loop region following their final *β*-strand (Fig. 2*b*), AAC(6′)-Ib has an additional helix (Fig. 2*a*) and AAC(6′)-Iy lacks the final strand, with the equivalent of strand S7 [*β*6 in AAC(6′)-Iy secondary-structure numbering; Vetting *et al.*, 2004] extended by an additional five residues relative to the other three enzymes and crossing over into the adjacent monomer in a location similar to the C-terminal strand in the other AAC(6′) enzymes.

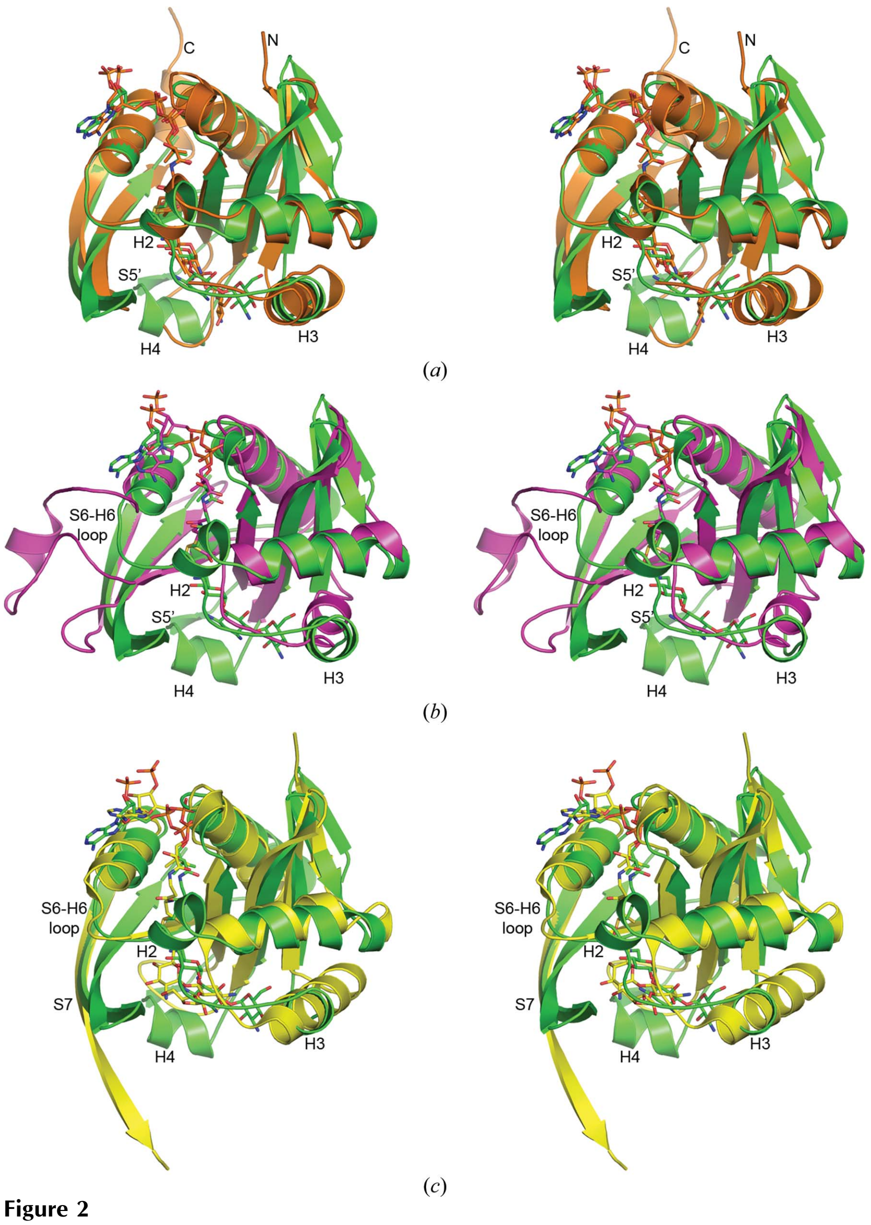

(*a*)

(*b*)

(*c*)

**Figure 2**

Stereoviews of the superposition of AAC(6′)-Ie onto three AAC(6′) enzymes. The regions showing large conformational variations between the structures are indicated in each panel. (*a*) AAC(6′)-Ie (green) and AAC(6′)-Ib (orange). (*b*) AAC(6′)-Ie (green) and AAC(6′)-Ii (magenta). (*c*) AAC(6′)-Ie (green) and AAC(6′)-Iy (yellow).

The other major structural differences are limited to four loop regions between secondary-structure elements (Fig. 1*c*). All four molecules differ quite markedly in the structure of an Ω-loop between strands S4 and S5, which in AAC(6′)-Ie comprises 16 residues folded as a short helix (H4) and a strand (S5′). The corresponding region in AAC(6′)-Ib (14 residues) and AAC(6′)-Iy (11 residues) is relatively unstructured, whereas in AAC(6′)-Ii it consists of only three residues. The other main differences occur in the polypeptide between H1 and H3, in the orientation of helix H3 and the loop between strand S6 and helix H6. Both AAC(6′)-Ie and AAC(6′)-Ib have a short helix (H2; Fig. 2*a*) between H1 and H3, while AAC(6′)-Ii and AAC(6′)-Iy have short loops (Figs. 2*b* and 2*c*). The conformation of the S6–H6 loop in AAC(6′)-Ie, AAC(6′)-Ib and AAC(6′)-Iy is essentially identical, comprising six residues (Figs. 2*a* and 2*c*); however, AAC(6′)-Ii has a major insertion of 24 residues which are predominantly unstructured except for a single turn of *α*-helix near the middle of the insertion (Fig. 2*b*).

### 3.2. Substrate and cofactor binding

AAC(6′)-Ie was pre-incubated with kanamycin prior to crystallization, and residual difference electron density consistent with a kanamycin molecule was evident in the initial maps calculated after molecular replacement (Fig. 3*a*). Also observed in the initial electron-density maps was a large extended piece of residual density consistent with the shape and location of coenzyme A

(CoA) or acetyl coenzyme-A (AcCoA) in other GNAT enzymes. Although no CoA or AcCoA was added to the enzyme prior to crystallization, the co-substrate was clearly present in both molecules in the asymmetric unit (Fig. 3*b*). A CoA molecule was added into the electron density in both molecules, and following subsequent refinement two residual electron-density peaks adjacent to the free thiol approximately 1.5 Å from the sulfur were observed (Fig. 3*c*). Two covalently bound O atoms were added and refined, with refined occupancies close to unity and sulfur–oxygen bond distances of between 1.50 and 1.55 Å. This was highly reminiscent of the electron density observed for oxidized cysteine residues, whereby two O atoms are covalently bound to a tetrahedral sulfur to give cysteine sulfinic acid (Becker *et al.*, 1998; Blackinton *et al.*, 2009; Nagashima *et al.*, 1998; Xu *et al.*, 2008). Sulfenic acid derivatives of CoA (a single oxygen bound to the sulfur) have been observed in protein structures (Jonsson *et al.*, 2004; Kato *et al.*, 2006; Mattevi *et al.*, 1993; Siehl *et al.*, 2007), in which a single O atom is covalently bound to the sulfur. In the present case, where we observe two full-occupancy covalently bound O atoms, this complex may represent the sulfinic acid form of CoA, which to our knowledge has never been reported before.

The oxidized CoA molecule binds to the exterior of the enzyme and projects through a positively charged tunnel in the molecular surface (Fig. 4*a*). The adenine moiety packs against the outside of helix H6 and the diphosphate group interacts with a glycine-rich loop at the N-terminus of H5. The pantothenate group passes through the tunnel formed by the inner side of helix H6, the C-terminus of helix S5 and the S5–H5 loop, and the thiol (and the transferable acyl moiety in the active AcCoA cofactor) projects out into the active site adjacent to the kanamycin. Supplementary Fig. S2 shows a schematic representation of the protein environment of the oxidized CoA and Supplementary Table S1 summarizes the hydrogen-bonding interactions. Comparison with other AAC enzymes for which structures have been determined with bound cofactors shows that although the oxidized CoA in AAC(6′)-Ie sits in essentially the same location, it does not necessarily adopt the same configuration. The conformation of the cofactor in AAC(6′)-Ie and AAC(6′)-Ib is very similar, with an r.m.s. difference in the positions of the matching atoms in CoA of 1.1 Å. In AAC(6′)-Ii and AAC(6′)-Iy, while the pantothenate and diphosphoshate moieties have the same configuration (r.m.s.d.s of 1.3 and 1.5 Å, respectively), the adenosine base on the exterior of both enzymes adopts a different configuration.

The kanamycin-binding site is on the opposite face of the *β*-sheet in a shallow highly negatively charged pocket in the molecular surface (Fig. 4*a*), with strands S4, S5 and the C-terminus of strand S6 forming the base of the pocket. The substrate is flanked by the C-termini of helices H2 and H3, strands S6 and S7, and helix H5, which form the walls of the depression (Fig. 4*b*). The A ring of the substrate containing the N6′ modification site is anchored by three hydrogen-bonding interactions to the main chain of Gly35 from the glycine-rich loop and the side chains of Asp136 and Glu163 (Supplementary Table S2), and by a hydrophobic face-to-face packing interaction with the side chain of Tyr34. The N6′ and O4′ atoms of the kanamycin also interact with one of the sulfinate O atoms of the oxidized CoA. The B ring has a single hydrogen-bonding interaction between the N3 atom and the side chain of Glu163 (Supplementary Fig. S2). The C ring packs against the C-terminus of helix H3, making three

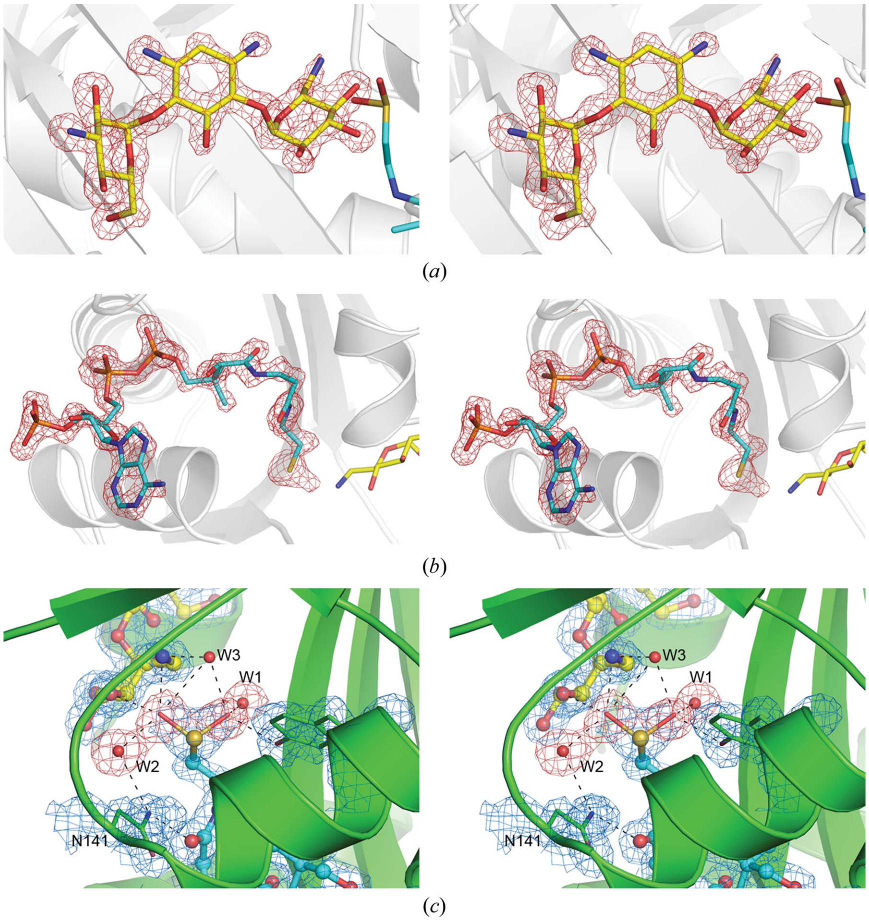

**Figure 3**
Electron-density maps for the ligands bound to AAC(6′)-Ie. (*a*) Kanamycin (yellow sticks) in the initial $F_o - F_c$ difference electron density (red) calculated following molecular replacement contoured at 3.0$\sigma$. (*b*) Oxidized coenzyme A (cyan sticks) in the initial $F_o - F_c$ difference electron density (red) contoured at 3.0$\sigma$. (*c*). Kanamycin (yellow sticks) and coenzyme A (cyan sticks) in $2F_o - F_c$ electron density (blue) at a 1.0$\sigma$ contour level calculated following 15 cycles of *REFMAC* refinement. Residual $F_o - F_c$ difference electron-density peaks (red) adjacent to the sulfur position are shown. The two thin sticks projecting from the S atom show the positions of two O atoms covalently attached to the sulfur from the final refined model, along with three closely associated water molecules (difference density for W3 is not shown).

hydrogen bonds to residues His49 and Glu52, two additional hydrogen bonds to the side chain of Gln74 from strand S4 and a hydrophobic interaction with the side chain of Trp54. The kanamycin molecule is surrounded by a network of water molecules, 16 in monomer *A* and 11 in monomer *B*, and a formate anion in both monomers. These interactions are summarized in Supplementary Fig. S2 and Supplementary Table S2.

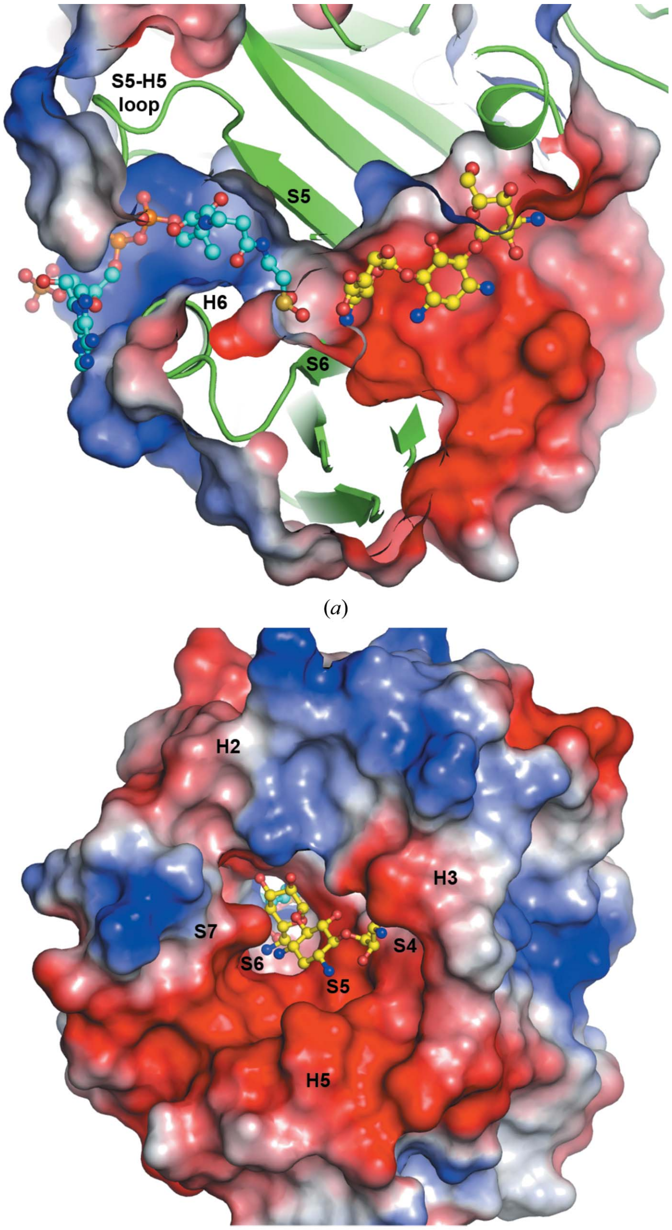

(*a*)

(*b*)

**Figure 4**
Molecular-surface representations of AAC(6′)-Ie showing the substrate- and cofactor-binding sites. (*a*) Cutaway view along the central $\beta$-sheet. The adenosine part of the oxidized coenzyme A (cyan ball-and-stick representation) is outside the molecular surface to the left. The diphosphate group and the pantothenate tail project through a tunnel in the surface of the molecule to position the S atom in the active site adjacent to the C-terminus of strand S6. The regions of the enzyme contributing to the formation of the tunnel (S5, the S5–H5 loop and H6) are indicated. The kanamycin (yellow ball-and-stick representation) is also shown. (*b*) A view down into the binding site for kanamycin (yellow ball-and-stick representation). The regions of the enzyme structure which contribute to kanamycin binding are indicated.

### 3.3. Small-angle X-ray scattering

The SAXS data of AAC(6′)-Ie and APH(2″)-Ia were analyzed for potential aggregation or intermolecular repulsion using the deviation from linearity in the Guinier plot at low *q* values. In the case of AAC(6′)-Ie the three lowest concentrations (0.5, 0.75 and 1 mg ml$^{-1}$) showed a consistent $R_g$ of 16.7 Å with a straight Guinier region down to the lowest *q* measured. The final curve for AAC(6′)-Ie was therefore merged using the 1 and 10 mg ml$^{-1}$ measurements (Supplementary Fig. S3). A similar Guinier analysis for APH(2″)-Ia resulted in a consistent $R_g$ of 21.7 Å for the two lowest concentrations (0.5 and 0.75 mg ml$^{-1}$); thus, the 0.75 mg ml$^{-1}$ data were merged with the 5 mg ml$^{-1}$ data to produce the final curve for further analysis (Supplementary Fig. S4). The final SAXS data for AAC(6′)-Ie and APH(2″)-Ia were subsequently compared with the calculated scattering intensities from the crystal structures using *CRYSOL* (Svergun *et al.*, 1995). In both cases the experimental data were in very good agreement with the calculated scattering profiles (Supplementary Figs. S3 and S4). Analysis of the Guinier region of the scattering curve for the bifunctional enzyme (Fig. 5*a*) showed no significant evidence of aggregation or inter-particle effects for the two lowest concentrations (0.5 and 0.75 mg ml$^{-1}$), giving a consistent $R_g$ of 29.9 Å. The Kratky representation of the scattering data (Supplementary Fig. S5) approaches the baseline at higher angles (>0.2 Å$^{-1}$), confirming that the full-length protein is well folded and does not sample a wide variety of conformational states in solution. This is in agreement with the previously reported SAXS experiments on the bifunctional enzyme (Caldwell & Berghuis, 2012). The pair distance distribution function $P(r)$ (Fig. 5*b*) was calculated with *GNOM* (Svergun, 1992) using standard settings and enforcing $P(r) = 0$ at $r = 0$ and $r = D_{\max}$. From this we obtained an estimated $D_{\max}$ of 94.7 Å and a real-space $R_g$ of 30.1 Å closely resembling that of the Guinier analysis. A set of 20 *ab initio* models were calculated using *GASBOR* (Svergun *et al.*, 2001) and subsequently superimposed and averaged with *DAMAVER* (Volkov & Svergun, 2003). The NSD value of the models ranged from 0.978 to 1.173 with a mean value of 1.10 as given by *DAMAVER*. The obtained shape model is shown in Fig. 5(*c*).

Rigid-body modeling calculations for the bifunctional enzyme using the crystal structures of AAC(6′)-Ie presented here and the recently reported APH(2″)-Ia structure (Smith *et al.*, 2014) connected by a flexible linker of variable length were performed using *CORAL* (Petoukhov *et al.*, 2012). A series of ten calculations were run with each of the linker lengths (zero, six, eight, ten and 12 residues) and repeated for three different starting orientations. In order to compare the results of the calculations, the APH domains of all the models were superimposed and the location and the orientation of the AAC domain was inspected. This analysis showed that all but a few of these calculations converged to a similar final orientation, giving an ensemble of conformations of the AAC domain with an angular spread in orientation of approximately 35° (Supplementary Fig. S6). An average representative conformation (using a six-residue linker) was used to calculate a *CRYSOL* scattering curve, which gives excellent agreement with the experimental data ($\chi$ = 2.4; Fig. 5*a*) and also aligns well with the results of the *GASBOR* calculation (Fig. 5*c*).

During the preparation of the models for the fitting procedure, care was taken to incorporate important factors related to the crystallographic models and what was known about the bifunctional enzyme, including prior information as to its possible structure in solution based upon the previously reported SAXS data (Caldwell & Berghuis, 2012). Since the AAC and APH domains represent the N-terminal and C-terminal portions of the full-length enzyme, the C-terminal residue of the AAC domain should necessarily be close to the N-terminal residue of the APH domain. The construct used in the expression of AAC(6′)-Ie ended at Tyr179 and the APH(2″)-Ia construct began at Met175 (Smith *et al.*, 2014), such that there is a five-residue overlap between the two domains (Fig. 6*a*). However, the N-terminal residues of the APH(2″)-Ia enzyme were unable to be modeled owing to a lack of electron density, with two of the four independent molecules beginning at residue Asp180 (numbered according to the sequence of the full-length enzyme) and the other two at Ala183 (Smith *et al.*, 2014). Monomers *A* from both AAC(6′)-Ie and APH(2″)-Ia were chosen as representatives for the two functional domains of the full-length AAC(6′)-Ie-APH(2″)-Ia enzyme. In the process of determining the lengths of the linker between the AAC and the APH domains, the C-terminus and the N-terminus of the AAC(6′)-Ie and APH(2″)-Ia structures, respectively, were analyzed in detail. The C-terminus of the AAC(6′)-Ie enzyme is very well defined in the electron-density maps (Fig. 1*a*), with atomic displacement parameters (ADPs) only slightly above the average ADP for the entire structure. The Tyr179 side chain itself is buried in an internal hydrophobic pocket formed by the side chains of Phe121, Val133 and Tyr177, and is protected from the external environment by the side chain of Lys125, which wraps across the phenolate ring (Fig. 1*a*). These interactions suggest that the C-terminus of the AAC(6′)-Ie molecule is highly constrained and, along with the preceding $\beta$-strand S8, would not be expected to show any significant flexibility irrespective of whether it is in the isolated AAC domain or in the intact full-length enzyme. Conversely, the N-terminus of the APH domain appears to be less constrained. The N-terminal $\alpha$-helix (helix A1) of APH(2″)-Ia, comprising residues 181–196, nestles against the N-domain $\beta$-sheet of APH(2″)-Ia. Analysis of the inner concave surface of the $\beta$-sheet and the corresponding inner surface of the helix shows that the areas of both which are in contact are highly hydrophobic and complementary in shape and structure (Fig. 6*b*), with the N-terminal end residues (180–185) being significantly more polar in nature and overhanging the $\beta$-sheet (Fig. 6*c*). This suggests that although the majority of the A1 helix (residues 186–196) is tightly associated with the $\beta$-sheet, the N-terminal five or six residues (180–185) might be somewhat less constrained and able to move. This is consistent with the kinetic studies on truncated forms of the bifunctional enzyme (Boehr *et al.*, 2004), where it was demonstrated the APH domain with the A1 helix removed (residues 195–479) lacks activity. Although helix A1 does not interact directly with the nucleotide- or substrate-binding sites, its dislocation from its observed position would expose a significant amount of hydrophobic surface. This may lead to destabilization of the $\beta$-sheet and adversely affect enzyme activity, as was observed with the truncated APH(2″)-Ia (Boehr *et al.*, 2004). Consequently, short linker lengths (zero, six, eight and ten residues), which did not require the

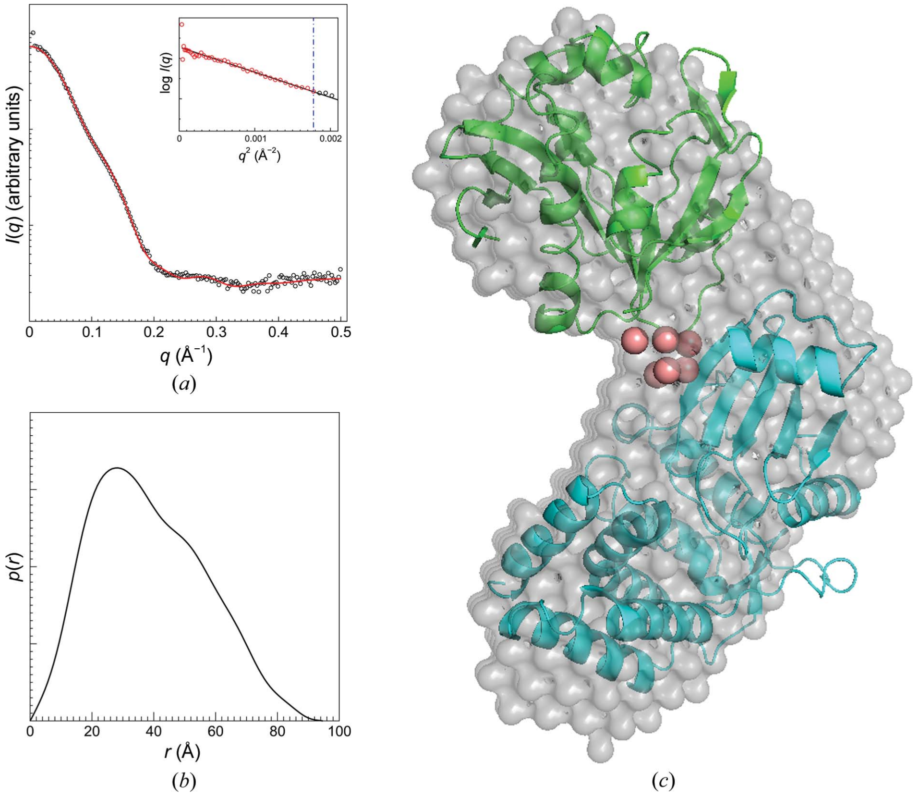

**Figure 5**
(*a*) Log-scale plot of the measured SAXS intensity *I*(*q*) for the bifunctional enzyme AAC(6′)-Ie-APH(2″)-Ia (open black circles). The solid red line depicts the *CRYSOL* fit of the rigid-body calculation using a six-residue linker ($\chi$ = 2.40). (*b*) Radial distance distribution function *p*(*r*) calculated using *GNOM*. (*c*) Superposition of the result of the rigid-body calculation using the crystal structures of AAC(6′)-Ie (green ribbon) and APH(2″)-Ia (cyan ribbon) connected by a six-residue flexible linker (red spheres) with the SAXS envelope calculated using *GASBOR* (gray beads).

unfolding of a large portion of the A1 helix, seemed to be more realistic than longer linkers, which would require the complete dissociation of the helix from the N-terminal $\beta$-sheet.

### 3.4. Modeling the bifunctional AAC(6′)-Ie-APH(2″)-Ia enzyme

The family of models generated by the rigid-body fitting of AAC(6′)-Ie and APH(2″)-Ia to the bifunctional SAXS data is shown in Supplementary Fig. S6. Although there appears to be a small degree of movement of the AAC domain relative to the APH domain (the maximum angular displacement between the two extremes of the rigid-body models is approximately 35°), the two domains sample a very tightly constrained region of dynamic space, with the average orientation represented by the model shown in Fig. 5(*c*). In this average representative model of the bifunctional AAC(6′)-Ie-APH(2″)-Ia, the AAC domain sits adjacent to the APH domain such that the $C^{\alpha}$ atoms of AAC(6′)-Ie Tyr179 and APH(2″)-Ia Asp180 are approximately 4.6 Å apart. Although care must be taken not to overinterpret the results given the low resolution of the SAXS data in comparison to the two crystal structures, we find it highly significant that despite the variation in the linker lengths used in the rigid-body modeling the orientation of the AAC domain relative to the APH domain remained very consistent and the N- and C-termini of the two domains remain within bonding distance of each other in the family of rigid-body models generated. In a test of the dependence of the starting orientations of the two structural domains on the rigid-body fitting outcome, a model composed of the APH(2″)-Ia and AAC(6′)-Ie structures with the AAC domain rotated such that the orientation of the domain resembled that described in the previously reported SAXS model (Caldwell & Berghuis, 2012) was generated. This model was subsequently used in additional rigid-body fitting calculations using linker lengths of zero, six, eight and ten residues. In all cases the final orientation of the AAC domain relative to the APH domain was consistent with the model shown in Fig. 5(*c*). Given the minimal level of variability in the orientation of the AAC domain, this would suggest that the full-length enzyme is relatively rigid in solution, as was suggested by the earlier SAXS studies (Caldwell & Berghuis, 2012). However, when compared with the previously reported model, the AAC domain in our model packs against the APH domain in an entirely different conformation (Fig. 7) that is rotated almost 180° such that the kanamycin-binding site of the AAC(6′)-Ie is on the opposite side of the molecule.

In the earlier SAXS model, crystal structures of AAC(6′)-Ib and APH(2″)-IIa were used to generate homology models of AAC(6′)-Ie and APH(2″)-Ia, respectively, for fitting to the SAXS data. Based on these calculations, it was suggested that the aminoglycoside-binding site of the AAC(6′)-Ie model was positioned adjacent to the aminoglycoside-binding site of the APH(2″)-Ia model. This led to the suggestion that a form of electrostatic channeling might be possible, in which substrate not modified in one of the active sites could readily diffuse into the active site of the neighboring domain, thus providing a slight enzymatic advantage to the close arrangement of the active sites. Although this is a very attractive hypothesis, given that there is no cooperativity or functional interaction between the two domains of AAC(6′)-Ie-APH(2″)-Ia (Boehr

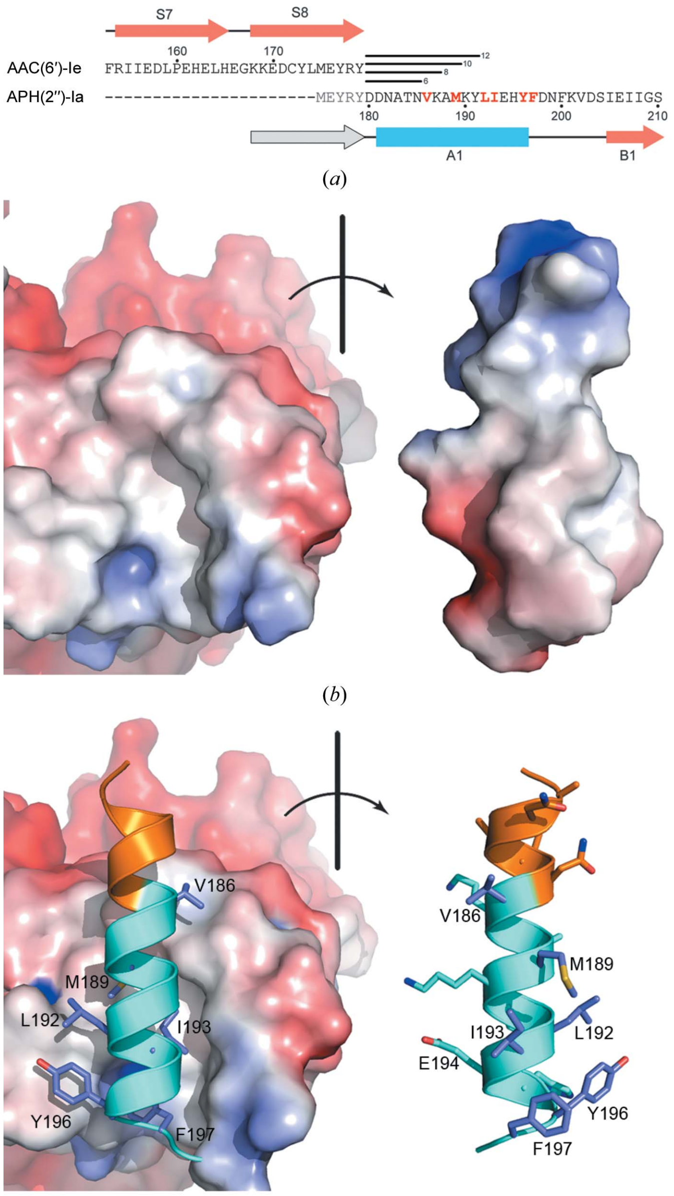

**Figure 6**
(*a*) The sequence of the bifunctional AAC(6′)-Ie-APH(2″)-Ia protein between residues 153 and 210. The individual AAC(6′)-Ie and APH(2″)-Ia sequences are separated for clarity and the residues which overlap between the two constructs are shown in gray [residues 175–179 in the APH(2″)-Ia sequence]. The linker lengths used in the rigid-body modeling of the bifunctional enzyme are indicated by black lines at the end of the AAC(6′)-Ie sequence. (*b*) Molecular-surface representation of the N-terminal domain of APH(2″)-Ia (left) with the N-terminal helix (residues 180–198) removed and rotated 180° about an axis in the vertical plane of the paper (right). (*c*) The same molecular surface as in (*b*) with the N-terminal helix removed from the surface calculation and reintroduced as a ribbon in its original location (cyan and orange; left). The hydrophobic residues are shown. The inner side of the N-terminal helix is shown on the right as a ribbon representation.

*et al.*, 2004; Martel *et al.*, 1983) there is no particular requirement that the two binding sites need to be close to each other. In fact, there may well be an advantage in the two sites being separated on opposite sides of the molecule, giving each site uninhibited access to the flux of substrate in the milieu without the possibility of any interference on substrate entrance into one site by an outgoing modified substrate molecule from the other, which could potentially occur were the two sites close to one another.

When the crystal structures of AAC(6′)-Ie and APH(2″)-Ia are used to reconstruct the AAC(6′)-Ie-APH(2″)-Ia model described in the earlier SAXS study, we note that Tyr179 of AAC(6′)-Ie is almost 30 Å from Asp180 of APH(2″)-Ia. Although the 17-residue linker used in the earlier study would readily bridge this distance, this would require the complete dislocation and possibly the partial unfolding of the A1 helix from APH(2″)-Ia which, based upon the known structure of the phosphotransferase domain, seems to be highly unlikely. The APH(2″)-IIa enzyme, upon which the APH(2″)-Ia homology model was based, has a somewhat shorter A1 helix and interacts with the N-terminal domain $\beta$-sheet in a different way such that the helix is angled at about 45° across the concave outer surface of $\beta$-sheet rather than directly along the cleft as in APH(2″)-Ia (Supplementary Fig. S7). Thus, the APH(2″)-Ia model derived from APH(2″)-IIa would have the A1 helix projecting in the wrong direction. The two other APH(2″) enzymes, APH(2″)-IIIa and APH(2″)-IVa, have A1 helices which more closely follow the path of the APH(2″)-Ia helix along the concave surface of the $\beta$-sheet, although in both cases these helices are at least a full turn or more shorter. The significant difference in the length and the path of the APH(2″)-IIa helix may explain the unrealistic location of the C-terminus of the AAC(6′)-Ie domain in the earlier SAXS model. In retrospect, either APH(2″)-IIIa or APH(2″)-IVa may have made better homology models for the initial SAXS interpretation, given the closer similarity of their A1 helices to that seen in the structure of APH(2″)-Ia (Smith *et al.*, 2014).

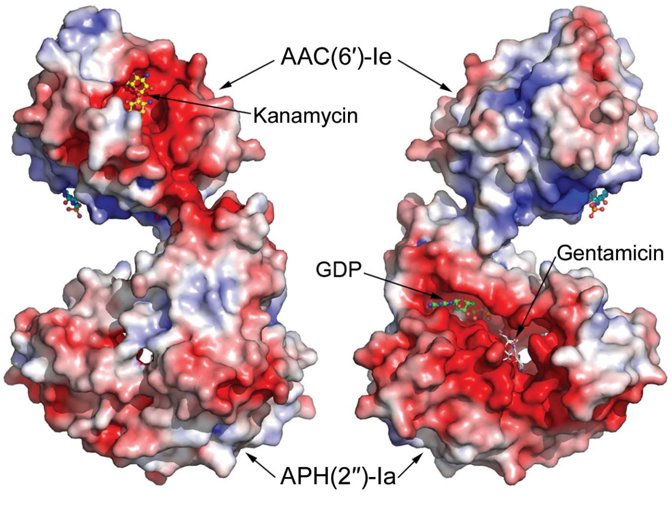

**Figure 7**
Electrostatic surface potential representation of the final bifunctional model with the AAC(6′)-Ie domain at the top and the APH(2″)-Ia domain at the bottom. (*a*) The model is in an orientation similar to that shown in Fig. 5(*c*). (*b*) The model rotated 180° about a vertical axis. The surface potentials range from $-5kT/\mathrm{e}$ (red) to $+5kT/\mathrm{e}$ (blue). The location of the kanamycin is shown as yellow ball-and-stick representation in the AAC domain and the adenine moiety of the oxidized coenzyme A is shown as a cyan ball-and-stick model just visible at the edge of this domain in both orientations. The location of a bound GDP molecule in the APH(2″)-Ia domain is shown in (*b*) as a green ball-and-stick model. The location of the aminoglycoside-binding site in the APH(2″)-Ia domain is indicated by the white ball-and-stick model, which represents a gentamicin from the APH(2″)-IIa structure (Young *et al.*, 2009).

## 4. Conclusions

The structure of the N-terminal domain of the important bifunctional antibiotic-resistance enzyme AAC(6′)-Ie-APH(2″)-Ia has been solved to 1.3 Å resolution. This domain, an acetyl coenzyme A-dependent aminoglycoside acetyltransferase, was crystallized as the kanamycin complex and was also found to have an oxidized form of coenzyme A in the binding site, giving rise to an abortive ternary complex. SAXS data measured for the two isolated AAC(6′)-Ie and APH(2″)-Ia domains shows that these independent molecules maintain their rigid structures in solution. Modeling of SAXS data measured from the bifunctional enzyme, using the N-terminal AAC(6′)-Ie domain and the C-terminal APH(2″)-Ia domain, shows that the full-length enzyme also exists as a predominantly rigid species in solution, although there is a small degree of movement of the two domains relative to each other. The two aminoglycoside-binding sites on the bifunctional enzyme are widely separated from each other, in contrast to the earlier SAXS model generated from homology models for the AAC and APH domains. The model generated from the SAXS data presented here places the binding sites on opposite sides of the molecule such that there would be no possibility of one antibiotic-binding site affecting the other, whether it be advantageous or adverse. This is consistent with biochemical and kinetic studies, which show no evidence for interactions between the two functionalities (Boehr *et al.*, 2004). The SAXS model also suggests that the long A1 helix at the N-terminal end of the APH(2″)-Ia domain plays a key role in the orientation of the two domains relative to one another, which further supports the premise that this linking helix is a key component in the overall stability of the bifunctional enzyme.

This work was supported by a grant from the National Institutes of Health: grant AI057393 (SBV). Portions of this research were carried out at the Stanford Synchrotron Radiation Lightsource, a national user facility operated by Stanford University on behalf of the US Department of Energy, Office of Basic Energy Sciences. The SSRL Structural Molecular Biology Program is supported by the Department of Energy (BES, BER) and by the National Institutes of Health (NCRR, BTP, NIGMS). The project described was also supported by Grant No. 5 P41 RR001209 from the NCRR, a component of the National Institutes of Health.

## References

Adams, P. D. *et al.* (2010). *Acta Cryst.* D**66**, 213–221.

Baker, N. A., Sept, D., Joseph, S., Holst, M. J. & McCammon, J. A. (2001). *Proc. Natl Acad. Sci. USA*, **98**, 10037–10041.

Becker, K., Savvides, S. N., Keese, M., Schirmer, R. H. & Karplus, P. A. (1998). *Nature Struct. Biol.* **5**, 267–271.

Berman, H. M., Westbrook, J., Feng, Z., Gilliland, G., Bhat, T. N., Weissig, H., Shindyalov, I. N. & Bourne, P. E. (2000). *Nucleic Acids Res.* **28**, 235–242.

Blackinton, J., Lakshminarasimhan, M., Thomas, K. J., Ahmad, R., Greggio, E., Raza, A. S., Cookson, M. R. & Wilson, M. A. (2009). *J. Biol. Chem.* **284**, 6476–6485.

Boehr, D. D., Daigle, D. M. & Wright, G. D. (2004). *Biochemistry*, **43**, 9846–9855.

Burk, D. L., Ghuman, N., Wybenga-Groot, L. E. & Berghuis, A. M. (2003). *Protein Sci.* **12**, 426–437.

Caldwell, S. J. & Berghuis, A. M. (2012). *Antimicrob. Agents Chemother.* **56**, 1899–1906.

Carter, A. P., Clemons, W. M., Brodersen, D. E., Morgan-Warren, R. J., Wimberly, B. T. & Ramakrishnan, V. (2000). *Nature (London)*, **407**, 340–348.

Cohen, A. E., Ellis, P. J., Miller, M. D., Deacon, A. M. & Phizackerley, R. P. (2002). *J. Appl. Cryst.* **35**, 720–726.

Davies, J. & Wright, G. D. (1997). *Trends Microbiol.* **5**, 234–240.

DeLano, W. L. (2002). *PyMOL*. http://www.pymol.org.

Dolinsky, T. J., Nielsen, J. E., McCammon, J. A. & Baker, N. A. (2004). *Nucleic Acids Res.* **32**, W665–W667.

Durante-Mangoni, E., Grammatikos, A., Utili, R. & Falagas, M. E. (2009). *Int. J. Antimicrob. Agents*, **33**, 201–205.

Dutnall, R. N., Tafrov, S. T., Sternglanz, R. & Ramakrishnan, V. (1998). *Cell*, **94**, 427–438.

Dyda, F., Klein, D. C. & Hickman, A. B. (2000). *Annu. Rev. Biophys. Biomol. Struct.* **29**, 81–103.

Emsley, P. & Cowtan, K. (2004). *Acta Cryst.* D**60**, 2126–2132.

Evans, P. (2006). *Acta Cryst.* D**62**, 72–82.

Ferretti, J. J., Gilmore, K. S. & Courvalin, P. (1986). *J. Bacteriol.* **167**, 631–638.

Hickman, A. B., Namboodiri, M. A., Klein, D. C. & Dyda, F. (1999). *Cell*, **97**, 361–369.

Jonsson, S., Ricagno, S., Lindqvist, Y. & Richards, N. G. (2004). *J. Biol. Chem.* **279**, 36003–36012.

Kabsch, W. (1993). *J. Appl. Cryst.* **26**, 795–800.

Karimi, R. & Ehrenberg, M. (1994). *Eur. J. Biochem.* **226**, 355–360.

Karplus, P. A. & Diederichs, K. (2012). *Science*, **336**, 1030–1033.

Kato, M., Wynn, R. M., Chuang, J. L., Brautigam, C. A., Custorio, M. & Chuang, D. T. (2006). *EMBO J.* **25**, 5983–5994.

Kim, C. & Mobashery, S. (2005). *Bioorg. Chem.* **33**, 149–158.

Krissinel, E. & Henrick, K. (2004). *Acta Cryst.* D**60**, 2256–2268.

Liu, P. (2009). *SasTool for Solution Data Analysis*. http://ssrl.slac.stanford.edu/~saxs/analysis/sastool.htm.

Martel, A., Masson, M., Moreau, N. & Le Goffic, F. (1983). *Eur. J. Biochem.* **133**, 515–521.

Mattevi, A., Obmolova, G., Kalk, K. H., Teplyakov, A. & Hol, W. G. J. (1993). *Biochemistry*, **32**, 3887–3901.

Maurice, F., Broutin, I., Podglajen, I., Benas, P., Collatz, E. & Dardel, F. (2008). *EMBO Rep.* **9**, 344–349.

Murshudov, G. N., Skubák, P., Lebedev, A. A., Pannu, N. S., Steiner, R. A., Nicholls, R. A., Winn, M. D., Long, F. & Vagin, A. A. (2011). *Acta Cryst.* D**67**, 355–367.

Nagashima, S., Nakasako, M., Dohmae, N., Tsujimura, M., Takio, K., Odaka, M., Yohda, M., Kamiya, N. & Endo, I. (1998). *Nature Struct. Biol.* **5**, 347–351.

Petoukhov, M. V., Franke, D., Shkumatov, A. V., Tria, G., Kikhney, A. G., Gajda, M., Gorba, C., Mertens, H. D. T., Konarev, P. V. & Svergun, D. I. (2012). *J. Appl. Cryst.* **45**, 342–350.

Ramirez, M. S. & Tolmasky, M. E. (2010). *Drug Resist. Updat.* **13**, 151–171.

Schatz, A., Bugie, E. & Waksman, S. A. (1944). *Proc. Soc. Exp. Biol. Med.* **55**, 65–69.

Siehl, D. L., Castle, L. A., Gorton, R. & Keenan, R. J. (2007). *J. Biol. Chem.* **282**, 11446–11455.

Smith, C. A. & Baker, E. N. (2002). *Curr. Drug Targets Infect. Dis.* **2**, 143–160.

Smith, C. A., Toth, M., Bhattacharya, M., Frase, H. & Vakulenko, S. B. (2014). *Acta Cryst.* D**70**, 1561–1571.

Smolsky, I. L., Liu, P., Niebuhr, M., Ito, K., Weiss, T. M. & Tsuruta, H. (2007). *J. Appl. Cryst.* **40**, s453–s458.

Stein, N. (2008). *J. Appl. Cryst.* **41**, 641–643.

Svergun, D. I. (1992). *J. Appl. Cryst.* **25**, 495–503.

Svergun, D., Barberato, C. & Koch, M. H. J. (1995). *J. Appl. Cryst.* **28**, 768–773.

Svergun, D. I., Petoukhov, M. V. & Koch, M. H. J. (2001). *Biophys. J.* **80**, 2946–2953.

Toth, M., Chow, J. W., Mobashery, S. & Vakulenko, S. B. (2009). *J. Biol. Chem.* **284**, 6690–6696.

Vagin, A. & Teplyakov, A. (2010). *Acta Cryst.* D**66**, 22–25.

Vakulenko, S. B. & Mobashery, S. (2003). *Clin. Microbiol. Rev.* **16**, 430–450.

Vetting, M. W., de Carvalho, L. P. S., Yu, M., Hegde, S. S., Magnet, S., Roderick, S. L. & Blanchard, J. S. (2005). *Arch. Biochem. Biophys.* **433**, 212–226.

Vetting, M. W., Hegde, S. S., Javid-Majd, F., Blanchard, J. S. & Roderick, S. L. (2002). *Nature Struct. Biol.* **9**, 653–658.

Vetting, M. W., Magnet, S., Nieves, E., Roderick, S. L. & Blanchard, J. S. (2004). *Chem. Biol.* **11**, 565–573.

Vetting, M. W., Park, C. H., Hegde, S. S., Jacoby, G. A., Hooper, D. C. & Blanchard, J. S. (2008). *Biochemistry*, **47**, 9825–9835.

Volkov, V. V. & Svergun, D. I. (2003). *J. Appl. Cryst.* **36**, 860–864.

Winn, M. D. *et al.* (2011). *Acta Cryst.* D**67**, 235–242.

Wolf, E., Vassilev, A., Makino, Y., Sali, A., Nakatani, Y. & Burley, S. K. (1998). *Cell*, **94**, 439–449.

Wybenga-Groot, L. E., Draker, K., Wright, G. D. & Berghuis, A. M. (1999). *Structure*, **7**, 497–507.

Xu, Z., Lam, L. S. M., Lam, L. H., Chau, S. F., Ng, T. B. & Au, S. W. N. (2008). *FASEB J.* **22**, 127–137.

Young, P. G., Walanj, R., Lakshmi, V., Byrnes, L. J., Metcalf, P., Baker, E. N., Vakulenko, S. B. & Smith, C. A. (2009). *J. Bacteriol.* **191**, 4133–4143.